Engineering Fracture Mechanics 321 (2025) 111111

Contents lists available at ScienceDirect

Engineering Fracture Mechanics

journal homepage: www.elsevier.com/locate/engfracmech

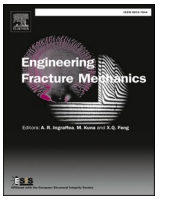

Fracture toughness behavior of high-Ni/high-Mn Barsebäck 2 reactor pressure vessel welds after 28 years of operation

Sebastian Lindqvist *, Noora Hytönen

VTT Centre for Nuclear Safety, Kivimiehentie 3, Espoo 02150, Finland

ARTICLE INFO

Keywords:
High Ni/Mn weld
Fracture toughness
Master Curve
Surveillance monitoring
Inhomogeneity

ABSTRACT

The safety assessment of reactor pressure vessels (RPV) is based on knowledge obtained from surveillance programs. In this study, the fracture toughness characteristics in the ductile-to-brittle transition region were determined for samples extracted from Barsebäck 2 RPV's beltline and head high Ni/Mn welds, and the results were compared to the surveillance welds. The fracture toughness results from the surveillance program describe the RPV core welds after 28 years of operation associated to a fluence of $0.1{\cdot}10^{19}$n/cm^2 in the beltline region. The results show that the microstructural features of the multilayer weld increase the uncertainty in the reference temperature T_0 to 34 °C. The inhomogeneity of the weld affects more the fracture toughness properties in comparison to impact toughness. The T_0 based embrittlement trend curve obtained for Barsebäck 2 weld subjected to a maximum fluence of $5.9{\cdot}10^{19}$n/cm^2 is compared to similar welds. The results contribute to improvements in reliability of aging management programs of nuclear power plants important for availability of carbon free energy.

fracture toughness decrease with radiation

1. Introduction

The reactor pressure vessel (RPV) is a life-limiting component in nuclear power plants (NPP). The operation margin reduces due to irradiation and thermal embrittlement [1]. As the fluence grows, hardness and strength increase, and the fracture toughness decreases. Surveillance programs monitor the effect of embrittlement on fracture and strength properties of the RPV.

The surveillance samples are extracted and tested in an established programs to ensure that the material properties sustain a sufficient margin for stable operation [2]. In the irradiation positions, the materials are typically located in azimuthal positions such that the capsules are subjected to a higher fluence compared to the RPV wall. The goal with the surveillance program is to form a predictive embrittlement trend curve to assess long-term operability [2–4]. The results from surveillance programs can be applied for validation of the analytical embrittlement trend curves developed in other programs. The embrittlement trend curves (ETCs) are usually analytical solutions dependent on chemistry and fluence [4]. The surveillance program includes the limiting RPV materials e.g. weld, heat-affected zone and base metals of the beltline region of the RPV [5]. Typically, the welds are subjected to a higher embrittlement rate due to higher impurity content. The life limiting location in the core region of an RPV is dependent on the absolute material properties and fluence levels in the vertical direction of the RPV.

In past investigations for materials extracted from decommissioned NPPs, the through-thickness properties of beltline welds have been characterized e.g. Novovoronezh unit 1, Midland unit 1, and Greifswald units 1, 4 and 8 [6–10]. These first NPPs did not include a

* Corresponding author.
E-mail address: Sebastian.lindqvist@vtt.fi (S. Lindqvist).

https://doi.org/10.1016/j.engfracmech.2025.111111
Received 3 December 2024; Received in revised form 2 February 2025; Accepted 3 April 2025
Available online 12 April 2025

Nomenclature

δ_i	Censoring parameter in the T_0 evaluation
a_0	Initial crack size
B	Thickness
E	Elastic modulus
F	Fluence
i	The running number by rank
J_C	J-integral at the onset of an instability
K_{Jc}	Stress intensity factor based on J_c
$K_{Jc,limit}$	The maximum K_{Jc} capacity of a specimen
MML	Multimodal Master Curve evaluation
N	Total number of specimens
P_{rank}	Rank probability
r	The number of qualified results
T	Temperature
T_0	Master Curve reference temperature
$T_{05\%eff}$	The T_0 providing the correct 5 % lower bound value in a MML evaluation
T_{28J}	Impact toughness-based transition temperature determined at 28 J
T_{41J}	Impact toughness-based transition temperature determined at 41 J
$T_{0,SINTAP}$	T_0 based on the SINTAP method
T_{0MML}	T_0 for a multimodal data set
T_{0Q}	Provisional T_0
W	Width
ν	Poisson's ratio
σ	Standard deviation
σ_{MML}	Standard deviation of T_0 in a MML evaluation

Abbreviations

ABLW	Axial beltline weld
ASTM	American Society for Testing and Materials ASTM International
B2	Barsebäck 2
BL	Baseline
C(T)	Compact tension
CBLW	Circumferential beltline weld
COD	Crack opening displacement
efpy	Effective full power years
ETC	Embrittlement trend curve
NPP	Nuclear power plant
RPV	Reactor pressure vessel
RPVH	RPV head
SC	Surveillance chain C
SG	Surveillance chain G

Table 1
Barsebäck 2 RPV. Additional details of the weld geometry and manufacturing are described in reference [11].

Parameter	Unit
Operation time	210 600 h at its peak operational pressure, equivalent to 22.7 effective full power years (efpy)
Reactor vessel head temperature	288 °C
Core region temperature	270°C
The RPV wall thickness in the beltline region	126 mm
The RPV head thickness in the beltline region	70 mm
Degradation mechanism: RPVH head	Thermal embrittlement
Degradation mechanism: Core region	Irradiation embrittlement at 270°C
Fluence after operation at the surface of the axial beltline weld trepan	$7.9 \bullet 10^{17} n/cm^2$ (E > 1 MeV)
Fluence after operation at the surface of the circumferential beltline weld trepan	$2.9 \bullet 10^{16} n/cm^2$ (E > 1 MeV)

[27,28]

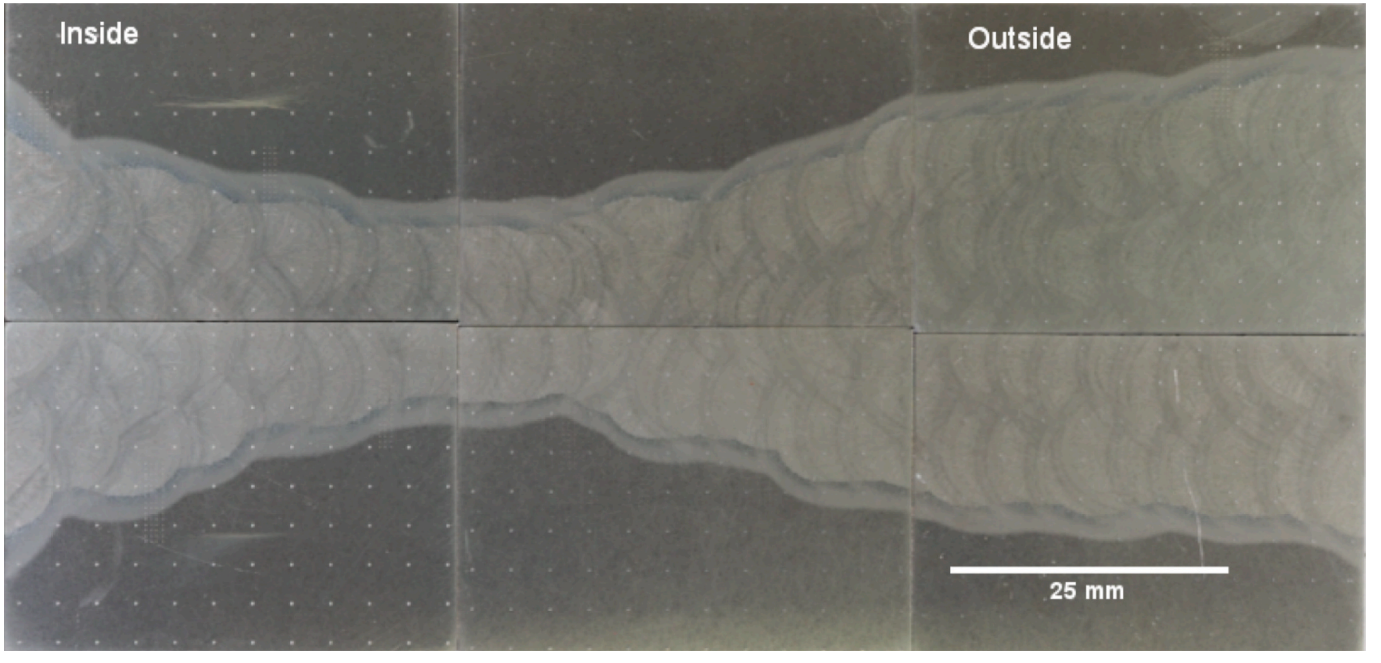

Fig. 1. Through-thickness cut of the Barsebäck RPV multilayer weld. The reheated regions form a web and surround the semi-circular as-welded regions.

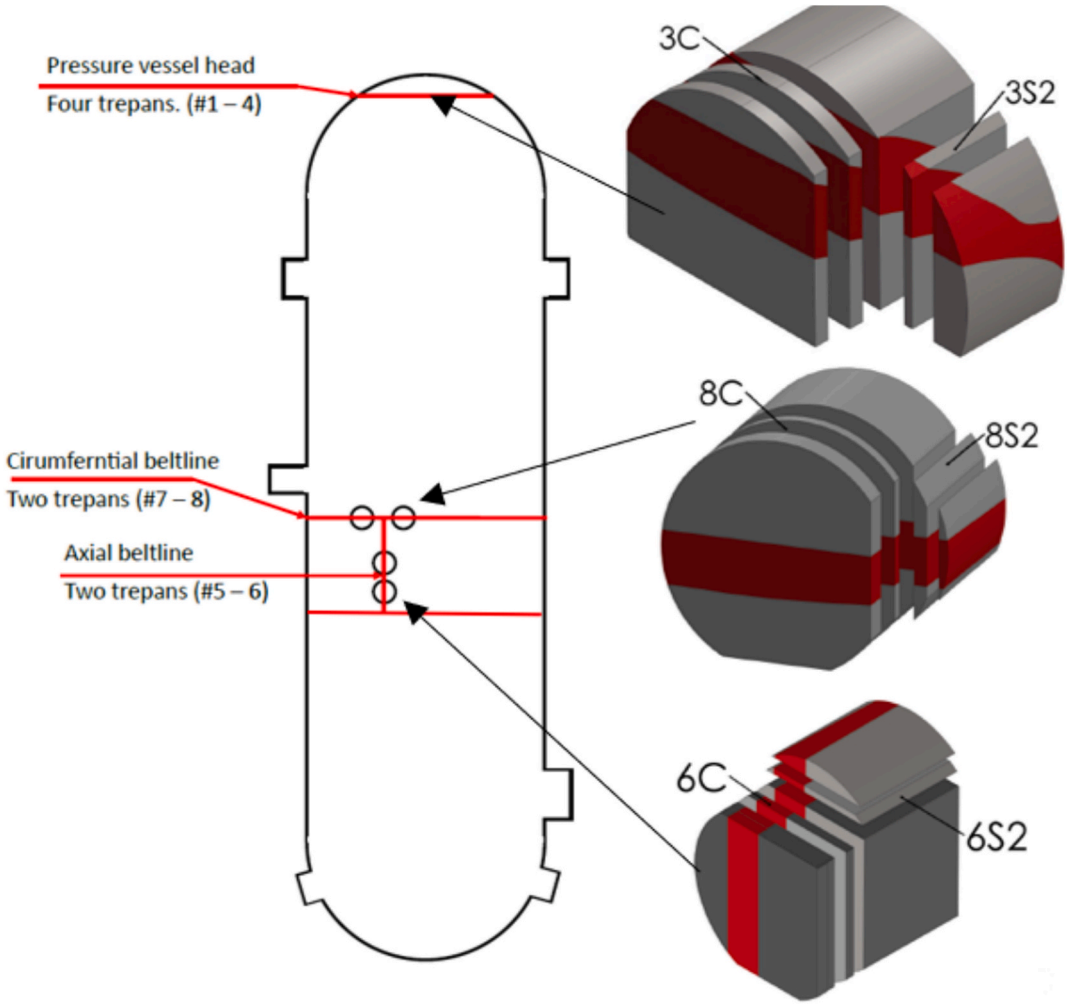

Fig. 2. Trepan extraction locations from Barsebäck 2 RPV. Red regions illustrate the weld seam in the trepan. The diameter of the trepan is 200 mm. (For interpretation of the references to colour in this figure legend, the reader is referred to the web version of this article.)

plant specific surveillance program. In a more recent project focusing on the Barsebäck 2 RPV welds, the results from the plant specific surveillance programs were compared to the aging of the decommissioned RPVs [11,12]. The comparisons are based on impact toughness and strength properties, and also the microstructural differences were characterized.

A characteristic feature for the Barsebäck 2 welds is the high Ni and Mn content. Previous published work on similar welds from Ringhals and VVER-1000 units focus on the surveillance data. Ringhals surveillance welds were manufactured using a similar chemical content as for Barsebäck 2 and the fracture toughness-based embrittlement curves indicate a 215 °C shift in reference temperature when the fluence is $8{\cdot}10^{19}$n/cm^2, E > 1 MeV [13,14]. The VVER-1000 welds have also a high Ni and Mn content but slightly higher Cr content. Various models have been developed for VVER-1000 welds, but for relatively low fluences [15,16].

Recently in an EU-project, STRUMAT (Structural materials for nuclear safety and longevity), the fracture toughness properties for irradiated steels with varying content of Ni/Mn were investigated [17,18]. The fluence range goes up to $11{\cdot}10^{19}$n/cm^2, E > 1 MeV, and the Ni and Mn content varies between 0.02 % − 2.0 % and 0.4 % − 1.4 %, respectively. Yet, none of these previous investigations focused on how the surveillance data describes the actual aging of the RPV.

High-Ni/Mn welds are sensitive to embrittlement due to the synergetic effects of Ni, Mn and Si [19]. The increased Ni content gives better hardenability and lower ductile-to-brittle transition temperature but increases the sensitivity of the material to radiation embrittlement [20]. The synergetic effect of Ni and Mn can become more significant after Mn content exceeds 0.8 % [19], and Ni content exceeds 1.3 % [21]. A relatively high temperature can also have a significant effect on the embrittlement rate for high Ni/Mn welds [22]. The current western ETCs are not applicable for high-Ni/Mn metals [23].

For some welds and base metals, the fracture toughness behaviour in the ductile-to-brittle transition region is on macroscopic level inhomogeneous [24,25]. This means that the scatter of the fracture toughness is larger than expected based on the normal Master Curve describing the characteristic scatter of fracture toughness for ferritic steels in the ductile-to-brittle transition region. In some orientations, the apparent inhomogeneity can be caused by use of small specimens [26]. Yet for welds, the macroscopic

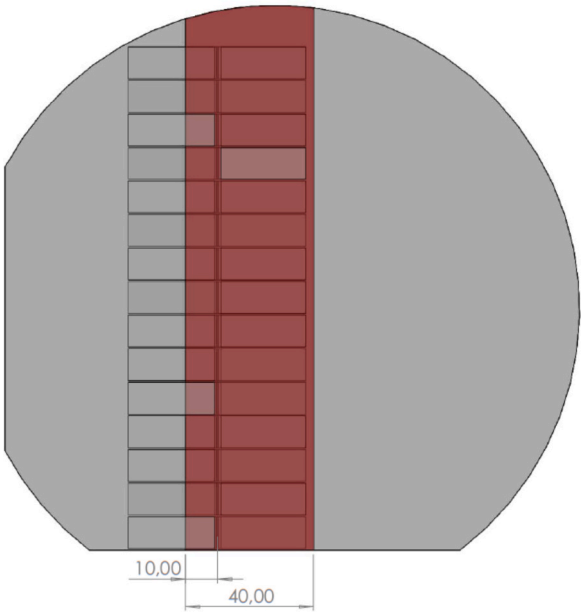

Fig. 3. Location of the impact toughness specimens cut form the sliced trepan. The facture toughness specimens were cut from the impact toughness specimen halves.

Table 2
Chemical composition (wt.%) of Barsebäck 2 welds.

Material	C	Si	Mn	P	S	Cr	Mo	Ni	Cu	Co	Al
Surveillance	0.084	0.22	1.53	0.011	0.004	0.13	0.44	1.47	0.06	0.008	0.005
RPVH	0.058	0.15	1.40	0.008	0.007	0.04	0.41	1.48	0.06	0.02	0.023
Axial BLW	0.054	0.16	1.43	0.010	0.005	0.03	0.44	1.66	0.07	0.02	0.022
Circ. BLW	0.064	0.16	1.43	0.008	0.005	0.03	0.44	1.66	0.09	0.02	0.078

inhomogeneities are a natural feature due to the solidification structure, but the degree of the inhomogeneity is situation dependent [24]. A Master Curve evaluation for macroscopically inhomogeneous materials has been developed and the extension is part of the ASTM E1921 testing procedure [23–25]. An inhomogeneity evaluation for fracture toughness data at different fluence levels can reveal new material behaviour trends. Noticeably, fracture toughness is more sensitive for macroscopic inhomogeneities compared to impact toughness. Most of the technical basis for current ETCs are based on impact toughness data.

In this study, the fracture toughness behavior of high-Ni/Mn welds from the decommissioned Barsebäck 2 RPV are compared to its surveillance welds. The welds were extracted from the RPV head, the circumferential and axial beltline welds at ¼ thickness location enabling comparison between the RPV head (RPVH) subjected to a high temperature (280 °C) and the beltline region subjected to

Table 3
Test matrix. Number of C(T) specimens, material state. The fluences for the axial and circumferential welds are given at the ¼ thickness location. Baseline weld is made from the same material as the other welds. All specimen were tested in T-S orientation. Yield strength values are determined at room temperature. The impact toughness results are from reference [11].

ID	Material	Material state	Number of specimens	Fluence [n/cm^2] (E > 1 MeV)	Flux [n/(s·cm^2)] (E > 1 MeV)	T_{28J} [°C]	T_{41J} [°C]	Yield strength [MPa]
BL	Baseline	Reference condition	12	0	–-	−85	−75	560
RPVH	Reactor pressure vessel head	23 efpy at 288 °C	20	0	–-	−85	−75	570
CBLW	Circumferential beltline weld	23 efpy at 270 °C + irradiation	15	$1.4•10^{16}$	$0.19•10^{8}$	−77	−70	580
ABLW	Axial beltline weld	23 efpy at 270 °C + irradiation	15	$3.8•10^{17}$	$5.2•10^{8}$	−106	−95	508
SC	Surveillance chain C	Irradiated at 270 °C	12	$0.102•10^{19}$	$14•10^{8}$	−78	−46	580
SG	Surveillance chain G	Irradiated at 270 °C	12	$5.87•10^{19}$	$809•10^{8}$	156	179	890

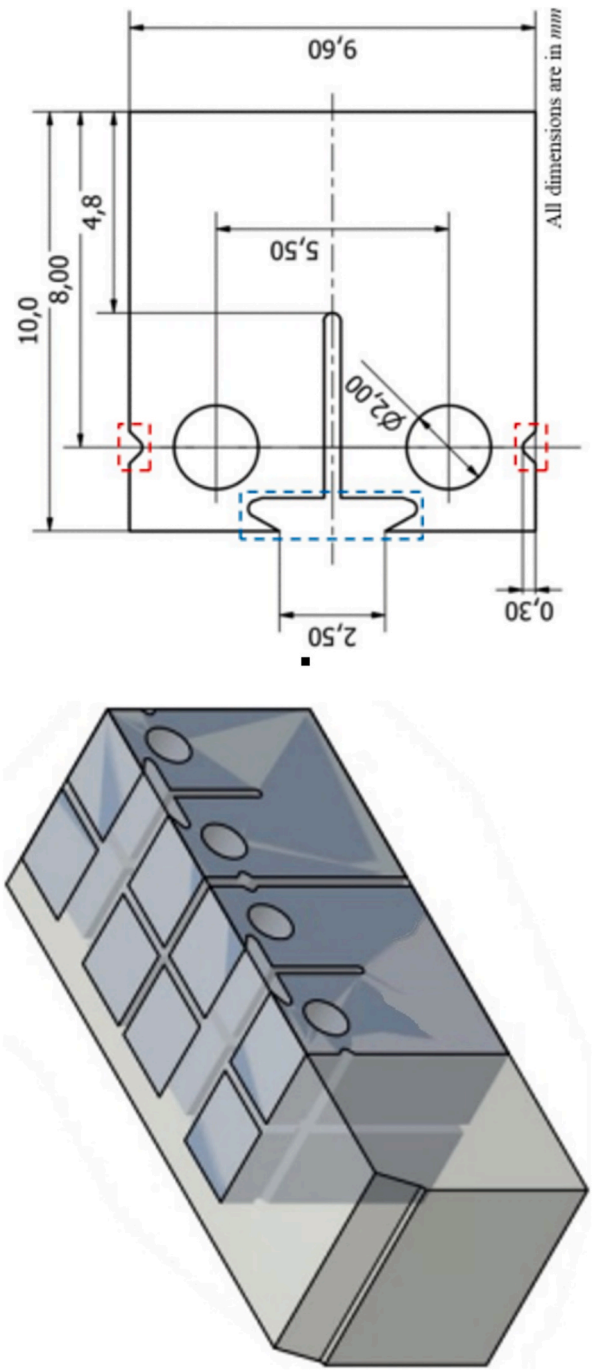

Fig. 4. Miniature compact tension specimens extracted from impact toughness specimens.

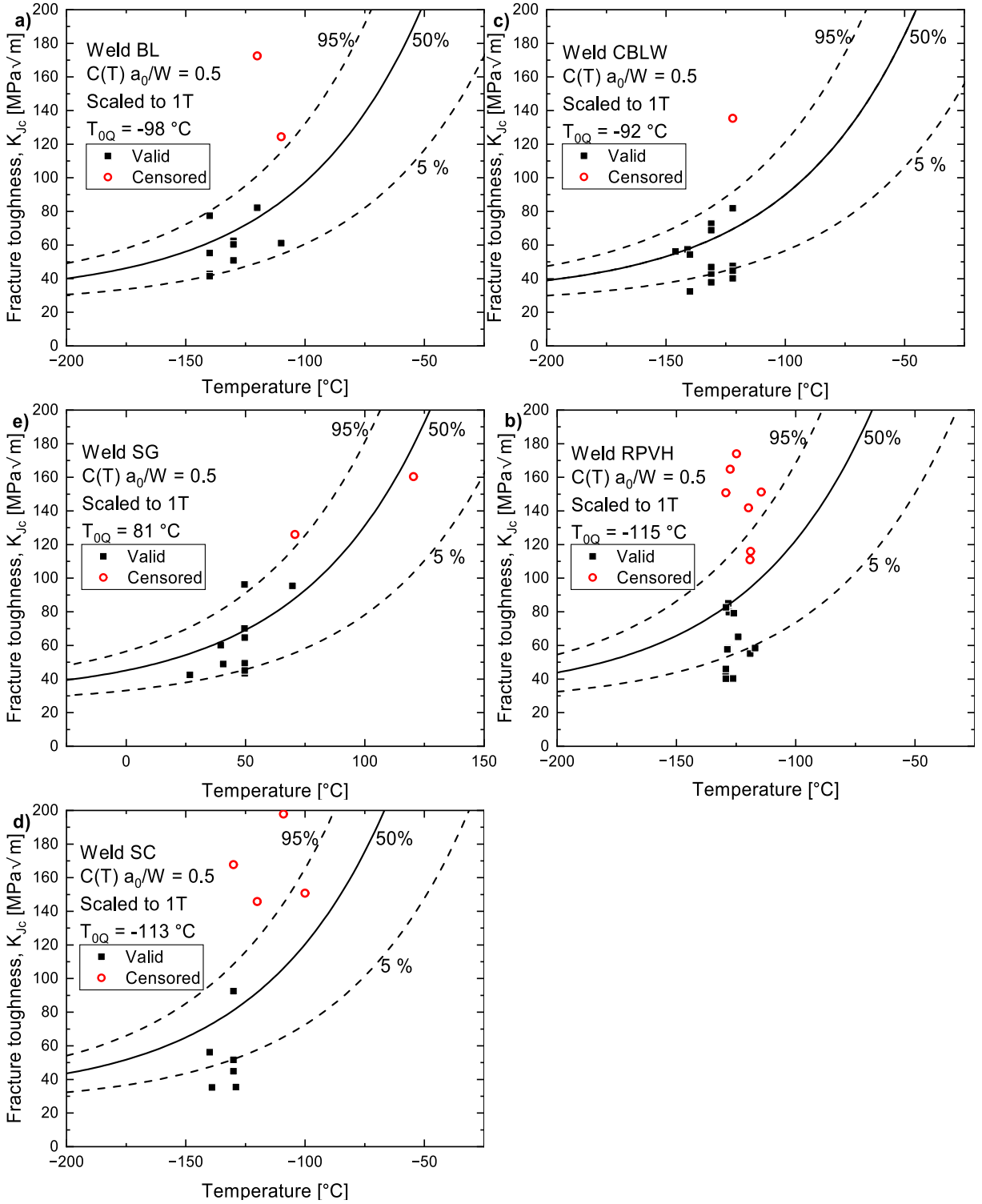

Fig. 5. Master Curves for baseline, RPV head, axial beltline, circumferential beltline, surveillance chain C and G welds.

irradiation and a similar irradiation temperature. The surveillance weld is manufactured using the same welding parameters and materials. The fracture toughness characterization for the welds was done following ASTM E1921 using the Master Curve procedure. The weld behavior is described through the most essential microstructural features. The results are also compared to impact toughness-based embrittlement curves to obtain understanding of the mechanisms related to brittle fracture. The inhomogeneity levels at

Table 4
ASTM E1921 assessment. The provisional T_{0Q} and the results from the inhomogeneity evaluation.

Material	T_{0Q} [°C]	Uncertainty, σ [°C]	r/N	Homogeneous	$T_{0,SINTAP}$ [°C]	$T_{0,MML}$ [°C]	σ_{MML} [°C]
BL	−98	7.2	10/12	No	−86	−91	22
RPVH	−115	6.4	13/20	No	−99	−106	40
CBLW	−92	6.7	14/15	No	−64	−74	32
ABLW	−102	6.6	13/15	No	−92	−95	21
SC	−113	8.2	7/12	No	−87	−101	46
SG	81	7.2	10/12	Yes	88	90	22
Combined data set $\Phi \leq 0.102 \cdot 10^{-19}$n/cm^2	−106	4.7	57/74	No	−88	−93	35
Combined T-T_0	0	4.7	67/86	No	12	12	34

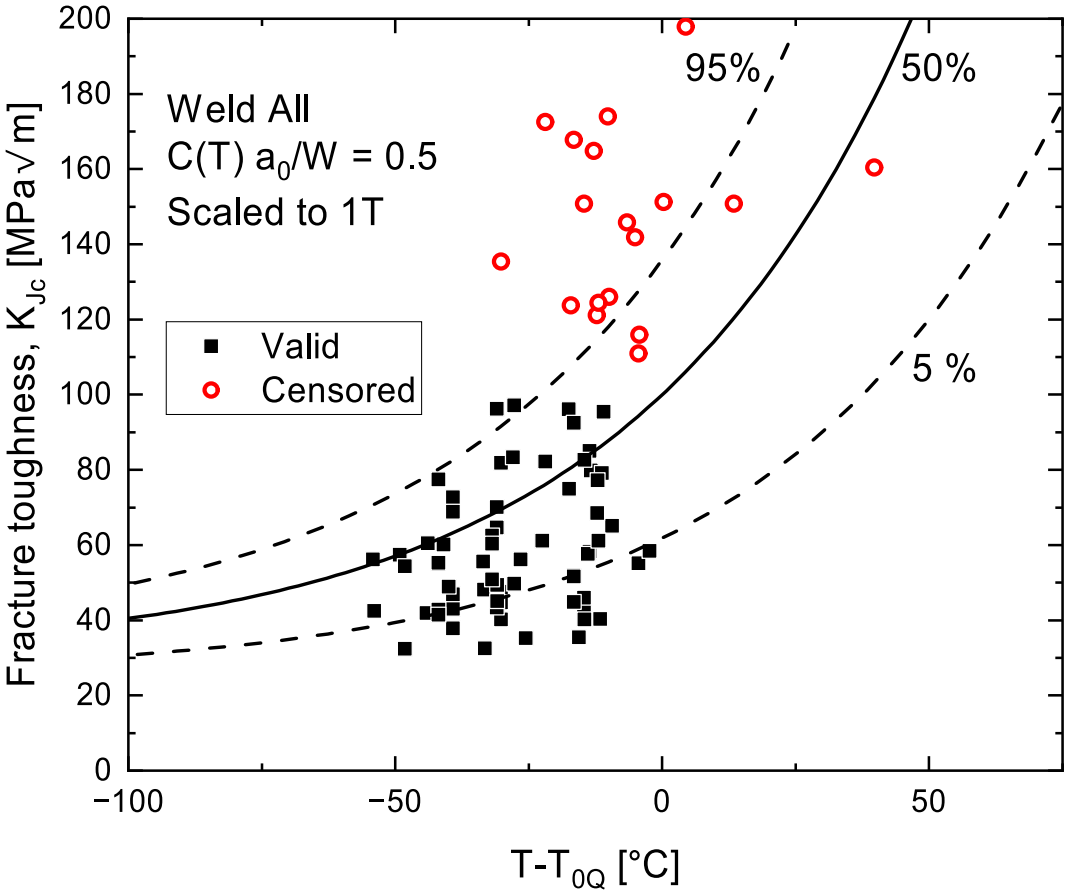

Fig. 6. Normalized fracture toughness data.

different fluences are also compared.

2. Materials and methods

This section presents the characteristics of the investigated welds and experimental program for characterizing the T_0 reference temperature. The investigation focuses on the extracted RPVH, axial and circumferential beltline welds and surveillance welds.

2.1. Materials

Table 1 shows some parameters for Barsebäck 2 RPV. All the RPV and surveillance welds were manufactured using same materials and welding procedure. The welds in different regions of the RPV are characterized by high-Mn/high-Ni content. The microstructure of the weld is characteristic for a multi-layer weld, see Fig. 1. The weld consists of as-welded regions with a dendritic microstructure and re-heated and twice re-heated regions with equiaxed microstructure caused by subsequent weld beads in the multi-layer weld [27,28].

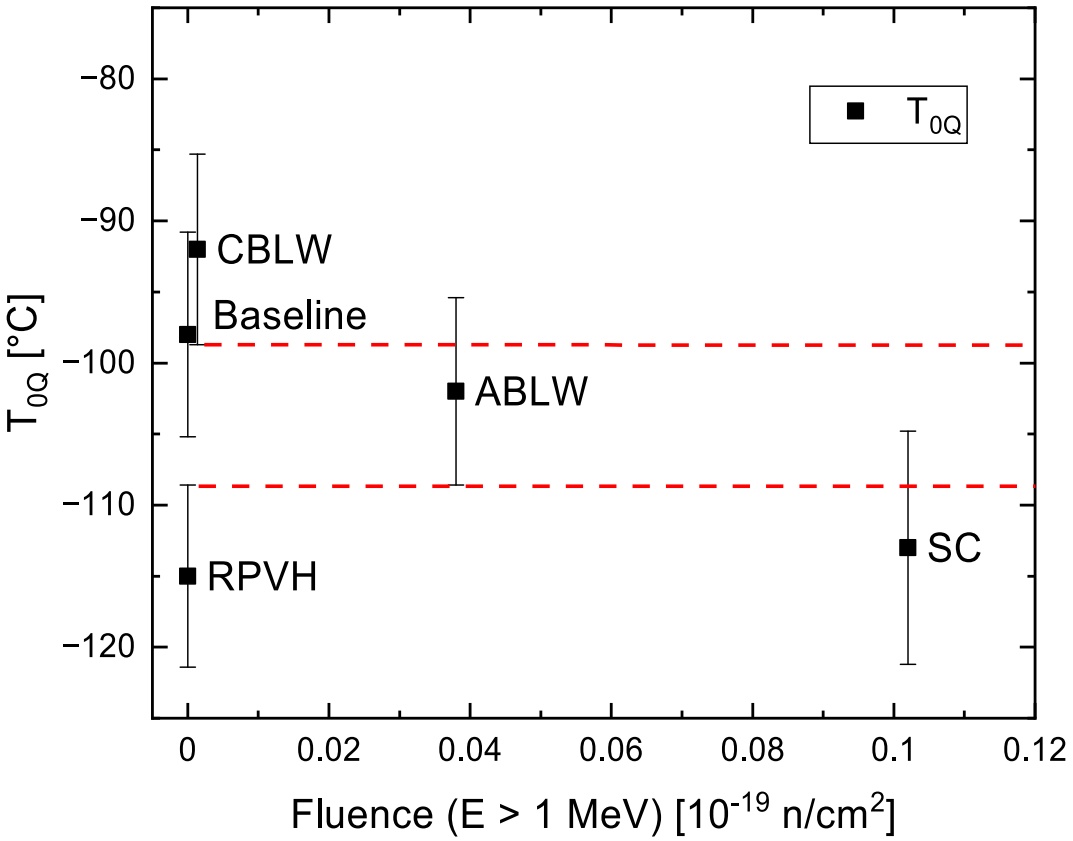

Fig. 7. Comparison of provisional T_{0Q} values. The error bars are based on one standard deviation.

Weld trepans were cut from the Barsebäck RPV head (RPVH), the axial and circumferential beltline welds, see Fig. 2. The trepans were cut into slices at the ¼ thickness location from where the fracture toughness specimens were cut, see Fig. 3. Table 2 gives the chemical composition for the welds. [27,28].

The plant contained also surveillance specimens. Eq. (1) follows the embrittlement rate of the surveillance weld. The surveillance weld is based on the same manufacturing procedures and materials as the RPV welds. Table 2 gives the chemical composition of the surveillance weld and the RPV welds.

$$\Delta TC_{V41J} = 57\left(\frac{F}{10^{19}}\right)^{0.287}, (\mathrm{E} > 1\,\mathrm{MeV}) \quad (1)$$

where ΔTC_{V41J} is the impact toughness-based transition temperature determined at 41 J and F (n/cm^2) is the fluence. The surveillance specimens were sampled at various through thickness locations of the manufactured surveillance weld. The surveillance specimen orientation is T-S—the crack grows in the thickness direction of the weld and the length of the specimen is transversal to the weld [11]. Table 3 gives the fluences and mechanical properties of the welds. The fluence of surveillance chain C materials is comparable to the beltline welds.

2.2. *Fracture toughness specimens*

The fracture toughness specimens conform to the requirements in ASTM E1921 [29]. The fracture toughness specimens were extracted in T-S orientation corresponding with the Barsebäck 2 surveillance program. All specimens cut from the trepans were extracted from the ¼ thickness location and the crack fronts sample the same through thickness location. The specimens were machined using electric discharge wire cutting and tested as manufactured. For the circumferential and axial beltline weld, the crack of the specimen was located closer to the center of the weld and the other fusion line (~10 mm). For the RPVH and surveillance weld, the crack was placed in both cases closer to the fusion line (~10 mm). Dimensions for the 4 mm thick (B) C(T) specimens, which are cut from tested Charpy specimens, are shown in Fig. 4. Recent work has focused on validating the testing procedure for 4 mm thick specimen for different materials [26,30–33].

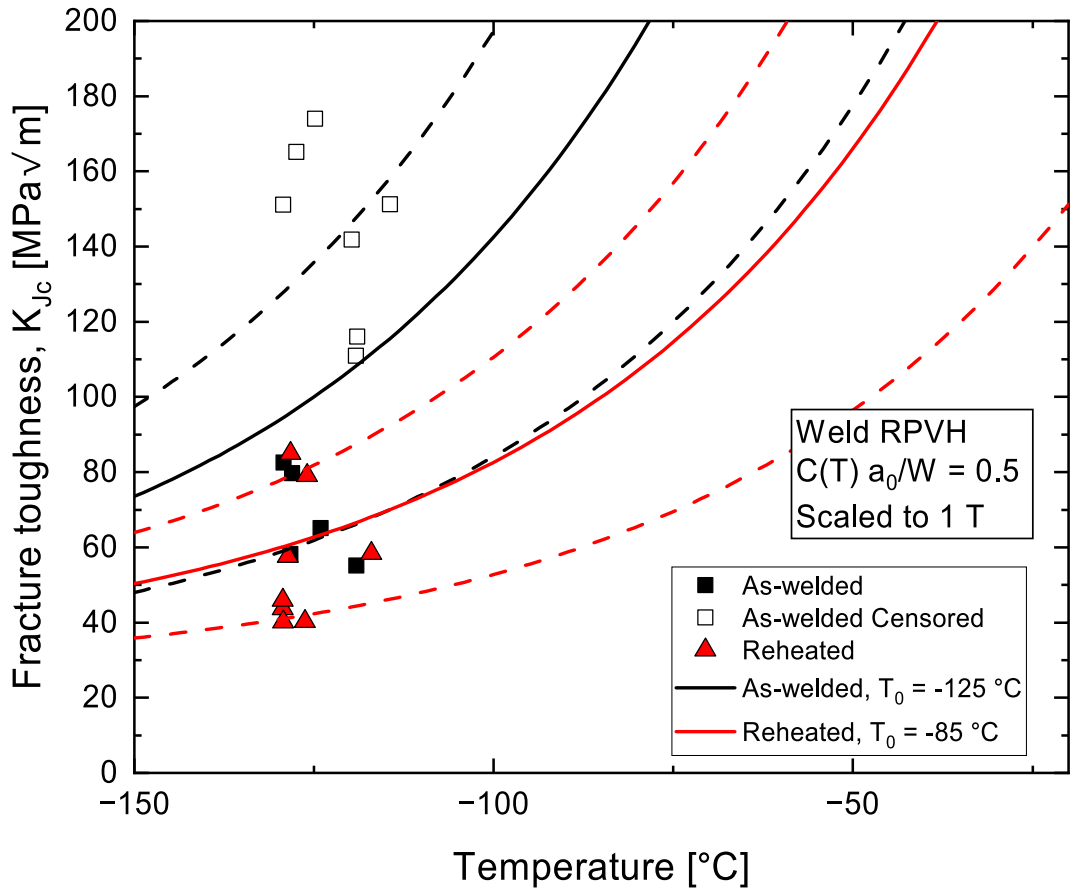

Fig. 8. Comparison of frature toughness of the as-welded and re-heated regions of the RPV head weld.

2.3. Fracture toughness testing

The fracture toughness tests and subsequent evaluation of reference temperature T_0 were performed in accordance with ASTM E1921 "Standard Test Method for Determination of Reference Temperature, T_0, for Ferritic Steels in the Transition Range"[29]. Before testing, the specimens were fatigue pre-cracked to the initial crack length over specimen width ratio, a_0/W, of 0.5. Front face type crack opening displacement (COD) measurement was applied (shown with blue dotted outline in Fig. 4b) during pre-cracking, while COD measurement from load line (shown with red dotted outline in Fig. 4b) was applied during fracture testing using Epsilon clip gauges.

All tests were conducted using Zwick Z250 universal testing machine equipped with thermal chamber. The C(T) samples were cooled using liquid nitrogen. The samples were broken post-testing, and the fracture surfaces were imaged. The crack lengths are measured according to the ASTM E1921. During testing, the force, CMOD and temperature were recorded. The loading rate was approximately 1 MPa$\sqrt{m}$/s. The CMOD-force curve was applied to calculate the fracture toughness, J_C or K_{Jc}, as described in ASTM E1921. Typical, CMOD-force curves are presented in Appendix 1. The quality of the data was assessed based on the standard. In the analyses, elastic modulus of 205 GPa and Poisson's ratio of 0.3 were used. Since the weld is inhomogeneous, the SINTAP [34] and Master Curve evaluations accounting for random inhomogeneities [25] were also applied for the data.

2.4. T_0 Master curve analysis

The Master Curve (MC) methodology enables characterization of ductile-to-brittle transition region using small specimens and less than 12 samples. The Master Curve relies on a theoretical description of the failure distribution for fracture toughness and an empirical temperature dependence for the ductile-to-brittle transition region [35]. The failure distribution and the temperature dependence are characteristic features for ferritic steels. The location of the Master Curve is parameterized by the reference transition temperature T_0.

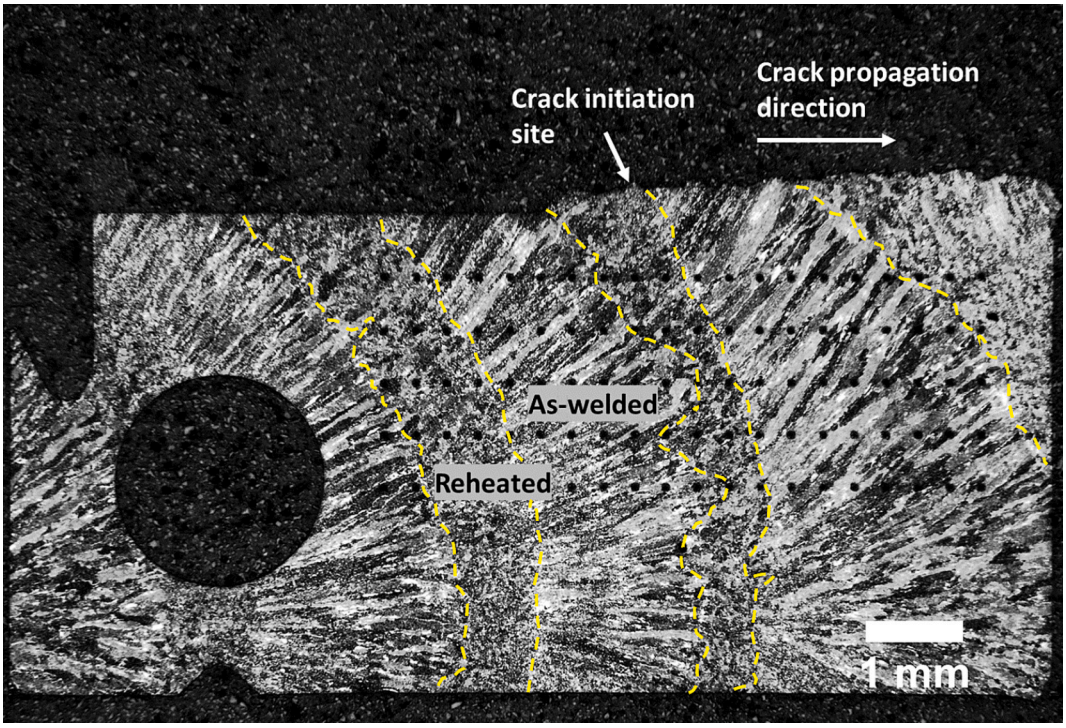

Fig. 9. Cross-section of a miniature C(T) specimen with a typical microstructure of the multilayer weld consisting of re-heated and as-welded regions. The fracture initiation site is indicated.

This methodology is adopted and described in ASTM E1921 [29].

The measured load and displacement data was used to calculate the fracture toughness at brittle fracture initiation, J_c, according to the equations in ASTM E1921. The J_c was converted to K_{Jc} using Eq. (2).

$$K_{Jc} = \sqrt{J_c \frac{E}{1-\nu^2}} \tag{2}$$

The results were size corrected to correspond to the stress intensity of 25 mm thick specimens using Eq. (3).

$$K_{Jc(25mm)} = 20\text{MPa}\sqrt{\text{m}} + (K_{Jc(B)} - 20\text{MPa}\sqrt{\text{m}}) \times \left(\frac{B}{25\text{mm}}\right)^{0.25} \tag{3}$$

where $K_{Jc(B1)}$ is the stress intensity factor of test specimen with a thickness of B_1. T_0 was determined with the maximum likelihood estimation, Eq. (4).

$$\sum_{i=1}^{n} \frac{\delta_i \bullet exp\{0.019 \bullet [T-T_0]\}}{11 + 77 \bullet exp\{0.019 \bullet [T-T_0]\}} - \sum_{i=1}^{n} \frac{(K_{Jc} - 20)^4 \bullet exp\{0.019 \bullet [T-T_0]\}}{(11 + 77 \bullet exp\{0.019 \bullet [T-T_0]\})^5} = 0 \tag{4}$$

where T_0 is the reference temperature, T_i is the test temperature, $K_{Jc(i)}$ is the measured stress intensity, and δ_i is 1 when the measured value refers to cleavage initiation and the measured K_{Jc} is smaller than $K_{Jc,limit}$, otherwise 0. The approximation of the median and average Master Curve, $K_{Jc(med)}$, for a 25 mm thick specimen, is determined with Eq. (5).

$$K_{Jc(med)} = 30 + 70exp[0.019(T - T_0)] \tag{5}$$

The 95 % (0.xx = 0.95) upper and 5 % (0.xx = 0.05) lower bounds of the Master Curve are calculated with Eq. (6).

$$K_{Jc(0.xx)} = 20 + \left[ln\left(\frac{1}{1-0.xx}\right)\right]^{1/4} \{11 + 77exp[0.019(T - T_0)]\} \tag{6}$$

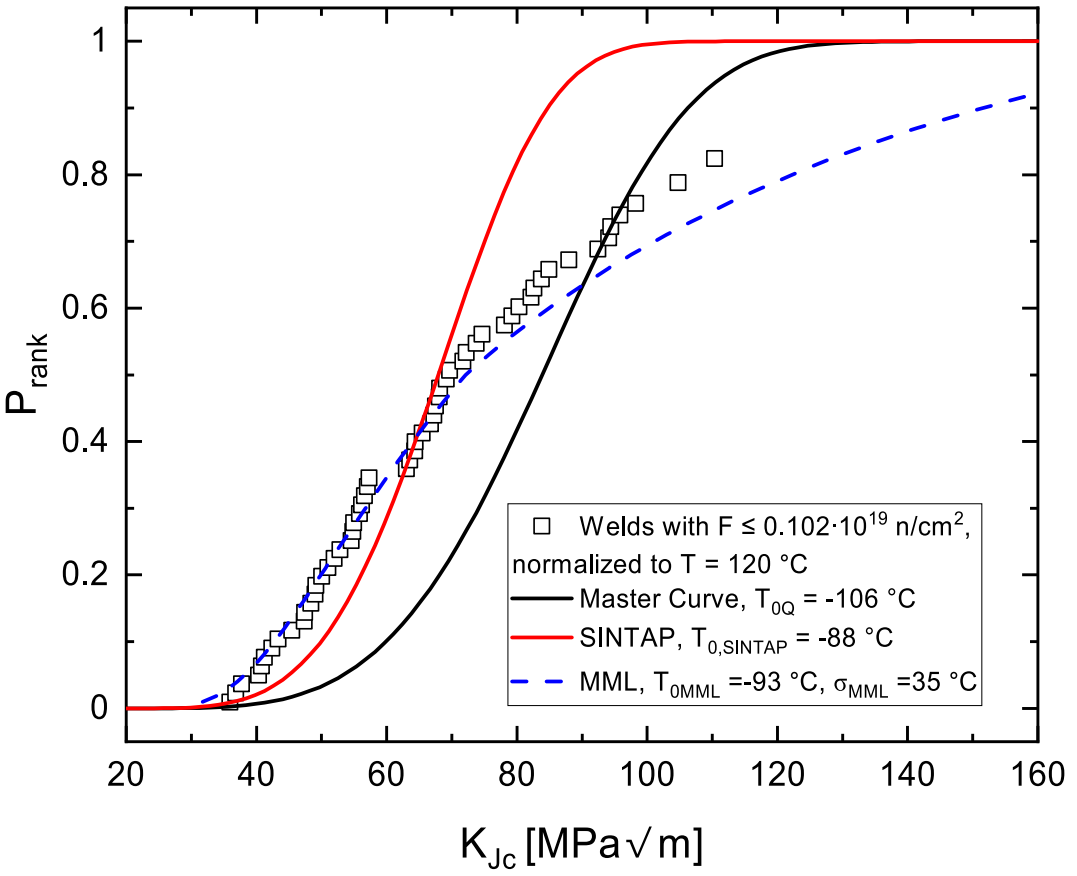

Fig. 10. Cumulative failure distribution of the normalized data in the low fluence region and the associated distributions based on the applied models.

After obtaining the provisional T_{0Q}, the results were screened according to the procedure in ASTM E1921 to check if the scatter is normal or the material behaves inhomogeneously on a macroscopic level. T_{0Q} represents the median of the results before inhomogeneity assessment. If the material is screened as inhomogeneous, then inhomogeneity evaluation methods described in ASTM E1921 are applied for characterizing the material. The inhomogeneity evaluation results in $T_{0,SINTAP}$ and the multimodal reference temperature parameters T_{0MML} and σ_{MML}. The $T_{0,SINTAP}$ determines the lower tail for a macroscopically inhomogeneous material. The MML method determines the whole failure distribution for a macroscopically inhomogeneous data set using the average T_{0MML} and the associated standard deviation σ_{MML}. The material is screened as macroscopically inhomogeneous if the difference between the T_{0Q} and $T_{0,SINTAP}$ is larger than the uncertainty of the method. The inhomogeneity evaluation procedure in described in detail in references [25,29]

3. Results

Fig. 5 shows the 5 %, 50 % and 95 % Master Curves for the welds. The qualified and censored results are shown. Censoring is done due to exceeding the $K_{Jc,limit}$. The amount of qualified results, r, in relation to the total number of specimens is given in Table 4. None of the results are disqualified due to exceeding the crack front curvature criterion, crack growth or compliance requirement. The table gives the provisional T_{0Q}, $T_{0,SINTAP}$, $T_{0,MML}$, σ_{MML} and final qualified T_0. All except surveillance weld G is screened as inhomogeneous. The tendency of the weld to behave inhomogeneously is shown Fig. 6 where the temperature is normalized with T_{0Q}. A relatively large portion of the results are below the 5 % Master Curve. The $T_{0,SINTAP}$ is applied as the final qualified value, but in later sections also the provisional T_{0Q} is applied in the evaluations. The results show that only surveillance weld G results in a significantly higher T_0.

Fig. 7 shows the difference between the provisional T_{0Q} values in the low fluence region ($< 0.102 \bullet 10^{19} n/cm^2$). The data in the figure shows the error bars based on one standard deviation. The uncertainty due to inhomogeneity is not accounted for in Fig. 7. The difference in T_{0Q} is largest between the circumferential and RPVH weld, 23 °C. The difference between the outer scatter bands of the circumferential and RPVH weld is 10 °C which is smaller than the σ_{MML} uncertainty factor due to inhomogeneity. Table 4 shows that

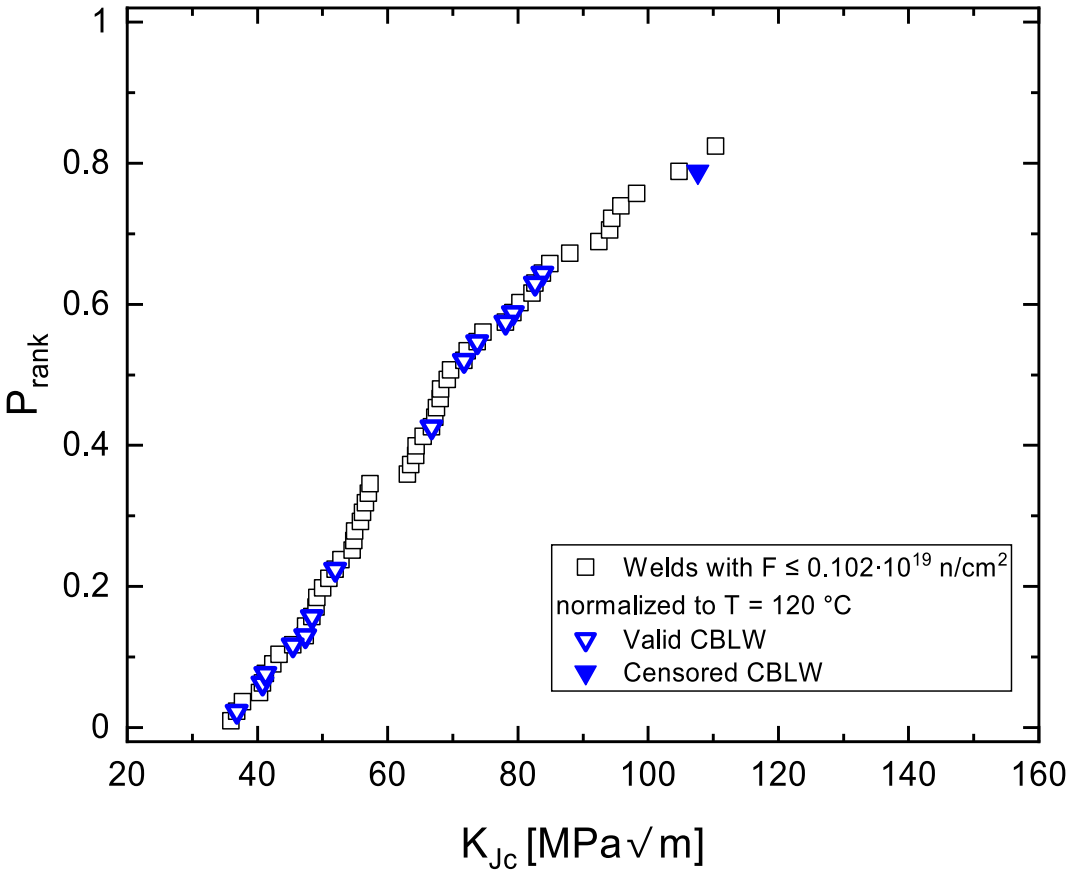

Fig. 11. Comparison of the distribution of the CBLW data to the other experimental results. The CBLW yields both high and low K_{Jc} values.

the σ_{MML} parameter is 34 °C for the normalized data. Consequently, due to the inhomogeneity, the differences in the results are insignificant in the low fluence region, and for that reason a combined T_0 value was calculated for the low fluence region, yielding a T_{0Q} of −106 °C.

4. Discussion

4.1. Effect of microstructure on inhomogeneity

Hytönen et. al [12,28] investigated the effect of microstructure on the observed inhomogeneity for the same RPV welds from Barsebäck 2 power plant. They cut the same fracture toughness specimens, characterized in this work, in two at the initiation site to observe the location of the crack-tip. By combining the observations to the fracture toughness results from this investigation, the results show that when the fatigue pre-crack tip of the fracture toughness specimens is located in the as-welded region, the T_0 is −135 °C and −85 °C if the tip is located in the re-heated region, see Fig. 8. Fig. 9 shows the multilayer structure of the weld. Klein et al. [36] investigated the influence of heterogeneity of the microstructure to toughness variations, discussing the change in probability of brittle fracture initiation depending on the location in the multilayer weld.

The variation in the fatigue pre-crack tip location within the multilayer weld explains the reason for screening the material as macroscopically inhomogeneous by the censoring procedure in ASTM E1921, Table 4. Besides the RPVH weld, the other welds are expected to be influenced equally by the same variation of the crack tip location. Due to the selected specimen orientation, the whole crack front can be located completely in the as-welded or reheated region. For other orientations, the probability that the whole crack front is located in a specific region is lower. The investigated orientation was selected since the original surveillance specimens were manufactured in this direction.

Fig. 10 presents the valid fracture toughness data points of the low fluence region ($F < 0.102 \bullet 10^{19} n/cm^2$) as rank probabilities. The K_{Jc} values are normalized to represent the fracture toughness at a given temperature and then ranked from lowest to highest. The rank probabilities are determined according to Eq. (7).

$$P_{rank} = \frac{i - 0.3}{N + 0.4} \tag{7}$$

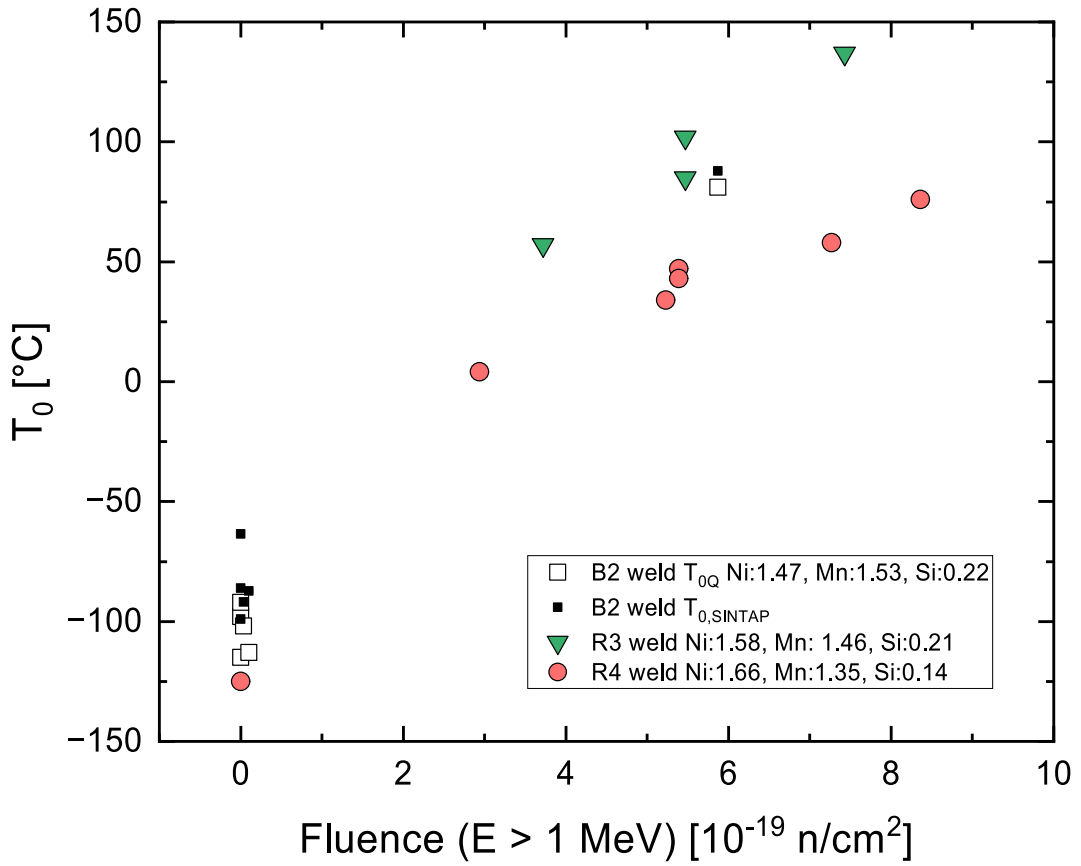

Fig. 12. Comparison of the embrittlement of the B2 weld to the R3 and R4 welds.

where i is the running number by rank and N is the total number of specimens (censored plus the valid data points). Presentation of the data as a cumulative failure distribution, P_{rank}-K_{Jc}, enables comparison of the applicability of the different Master Curve approaches (normal Master Curve, MML, SINTAP) to describe the data.

The cumulative failure distribution of the normal Master Curve gives an unconservative description for the probabilities in the lower tail e.g. at $P_{rank} = 0.2$ the experimental data gives $\sim$ 50 MPa$\sqrt{m}$ whereas the Master Curve yields a $\sim$ 20 MPa$\sqrt{m}$ larger value. The SINTAP procedure describes more accurately the lower tail, and the difference to the measured values is less than the uncertainty of the Master Curve method. The MML method overlaps with the experimental data.

In the low fluence region, the differences between the $T_{0,SINTAP}$ values are small for BL, RPVH, ABLW and CS, maximum difference being 13 °C. The CBLW weld results in a 20 °C higher value. Due to a lower fluence in relation to the ABLW and SC welds, the effect of irradiation is weaker for the CBL weld and that should not be an explaining factor for the difference. For the CBLW weld, the ratio of specimens sampling the microstructural constituents resulting in a lower fracture toughness can be higher. Fig. 11 shows that only one CBLW fracture toughness values is above $P_{rank} = 0.7$.

The inhomogeneity screening indicates that surveillance weld G, $F = 5.87 \bullet 10^{19} n/cm^2$, is homogeneous. In theory, irradiation could even out the difference in fracture toughness observed between the re-heated and as-welded regions. However, the screening result is on the boarder of being categorized as inhomogeneous as the difference between T_{0Q} and $T_{0,SINTAP}$ is 7 °C, almost larger than the uncertainty. In addition, the σ_{MML}, a measure for inhomogeneity, indicates that the level on inhomogeneity is at the same level as for the other conditions. SCG weld is thus treated similarly to the other welds and the final qualified T_0 is based on $T_{0,SINTAP}$.

4.2. Comparison of the surveillance results to the aging behavior of the RPV welds

When comparing the baseline and surveillance results in the low fluence region to the results of the extracted welds from the reactor pressure vessel, the results overlap as described in section 3. Consequently, the surveillance weld describes the aging behavior of the actual RPV welds in the low fluence region. Future work could focus on similar validation of the surveillance program for higher fluences.

In the low fluence region, at a fluence of $0.102 \bullet 10^{19} n/cm^2$, the shift in impact toughness based T_{41J} is 29 °C $\pm$ 2σ = 16 °C indicating a significant impact of embrittlement on mechanical properties, see Table 3 and reference [11]. Due to the natural difference

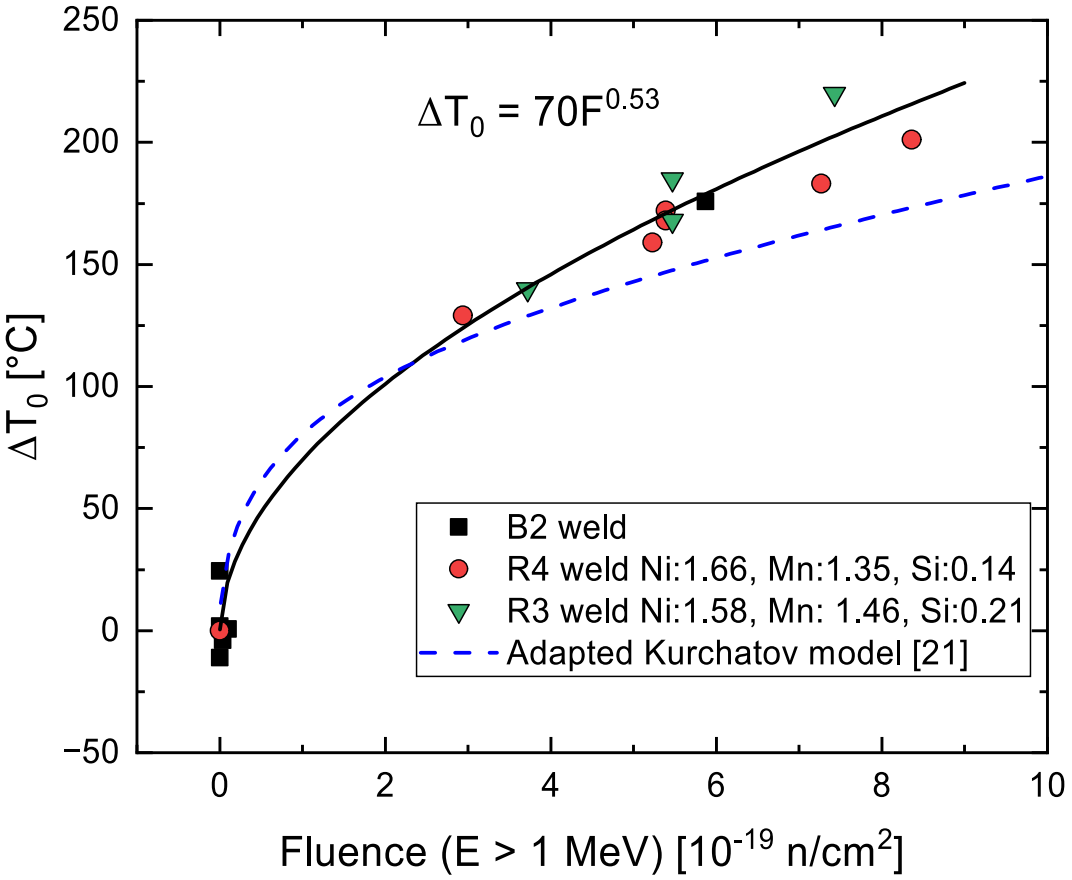

Fig. 13. Comparison of the embrittlement rate of the B2 weld to the R3 and R4 welds.

between impact and fracture toughness testing, the measured embrittlement rate can differ, as will be discussed later. In general, the T_{28J} and T_{41J} values presented in Table 3 for Barsebäck 2 welds are consistent, transition temperature increases with the fluence, except for the axial beltline weld. Only the axial beltline weld results in a value 20 °C lower compared to the non-irradiated condition, even if an increase in the transition temperature can be expected as the fluence is $3.8 \bullet 10^{17}$n/cm^2. In [11], the post-weld heat treatment (PWHT) procedure was given as a possibility for explaining the difference. Although, based on non-published work for the same materials, the differences in PWHT are not necessarily significant for these welds, indicating that the explaining factor for the difference is the natural variations in the material resulting from multiple factors during manufacturing.

The trends based on the impact toughness specimens in the low fluence region described above are not evident based on the facture toughness results. The scatter is larger due to the nature of the test type and the inhomogeneity of the weld can have a larger impact. The results indicate that the possible variations in fracture toughness due to irradiation in the low fluence region are smaller than the uncertainty of the method and the material.

4.3. Embrittlement trends

Fig. 12 compares the T_0-fluence embrittlement trends to the results from the Ringhals 3 and 4 surveillance programs [14]. As the fluences are high, only the surveillance chain G results from B2 are essential for this comparison. The Ni, Mn and Si contents of the Ringhals welds are similar to the B2 welds characterized in this study, as shown in the Fig. 12 labels. The mentioned elements and especially Ni and Mn control the embrittlement rate for high-Ni steels [16,23,37]. The Ni, Mn and Si composition of the B2 weld is closer to that of the R3 weld. The B2 results are closer to the R3 results when fluence is $6 \bullet 10^{19}$n/cm^2, the difference being 10–20 °C. On the other hand, Fig. 13 indicates that a common ETC can be generated for the three welds. The R4 and R3 investigations were performed using 5x10 SE(B) specimens and the orientation is T-L, different compared to this study.

The Kurchatov model developed based on surveillance data for VVER-1000 base and weld metals with high Ni and Mn content gives a decent estimate of the embrittlement behavior in the investigated range considering that the model is developed for lower fluences and the Cr content is higher, see Fig. 13 [15]. At higher fluences, the model underpredicts the measured shift. The Ni and Mn contents are similar. The Kurchatov model is based on impact toughness and thus the result was converted to ΔT_0 using Eq. (8) [18]. The Kurchatov model was applied using the following parameters; average Ni content is 1.62 %, Mn content is 1.4 %, T_{KO} is −104 °C, and

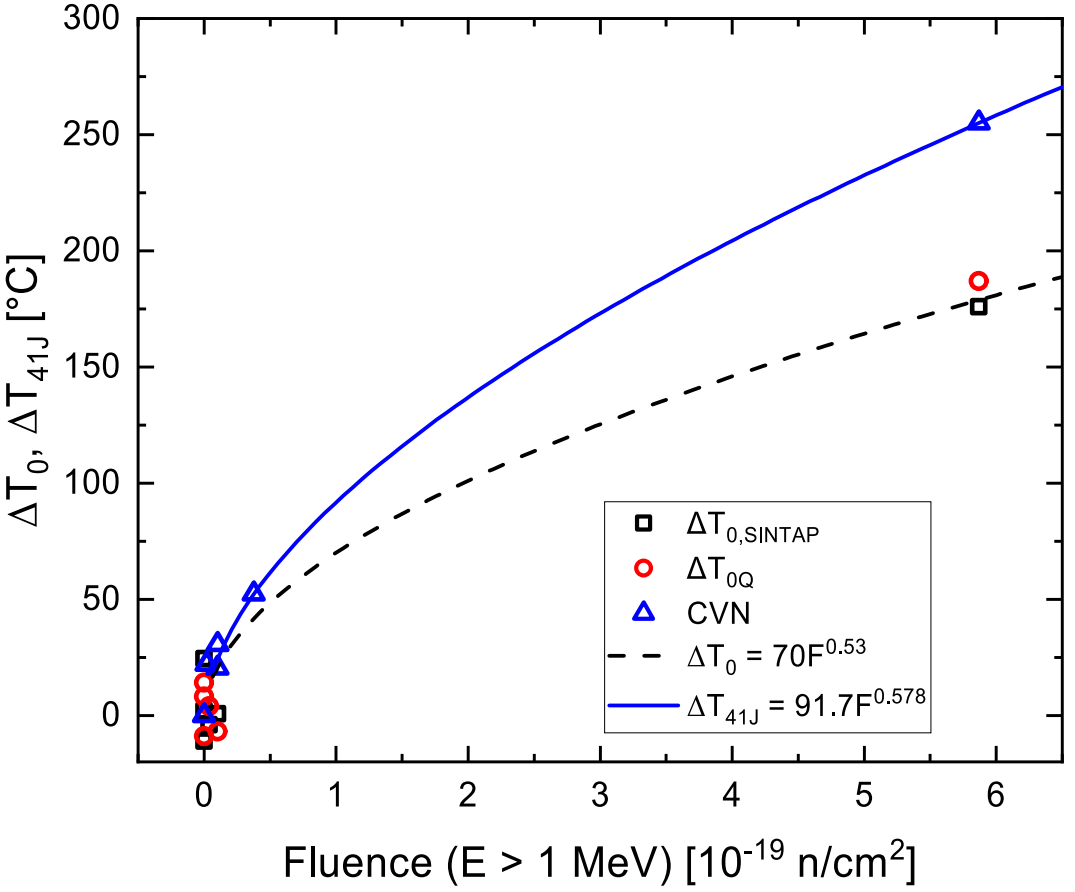

Fig. 14. Comparison of the embrittlment curves for B2 welds dependent on fracture toughness-based T_0 and impact toughness-based T_{41J}.

the fluence of $5.87 \bullet 10^{19}$n/cm^2 was reached in 23 years. The ratio between neutron energies of E > 1 MeV and E > 0.5 MeV is 1.78 [21].

$$\Delta T_0 = 4\Delta T_{41J}{}^{0.68} \tag{8}$$

4.4. Correlation between fracture and impact toughness

Fig. 14 compares the shifts in T_0 and T_{41J} of the B2 weld. The result shows that the difference is larger at $5.87 \bullet 10^{19}$n/cm^2 compared to the low fluence region. Impact toughness is dependent on changes in the crack propagation and arrest properties [35,38]. Crack propagation in impact toughness specimens is affected by the reduction upper shelf energy due to irradiation embrittlement, but it does not explain the whole difference at large fluences [18]. The weakening of the matrix due to aging in combination with the elemental changes at the grain boundaries can affect more crack propagation and arrest energies compared to the fracture initiation event [38]. Fracture toughness based T_0 is dependent on the initiation event.

Fig. 15 shows the difference between the measured T_0 and predicted T_0 based on impact toughness, see Eq. (9).

$$T_{0,CVN}(T_{28J}) = T_{28J} - 18 \tag{9}$$

The closer the result is to 0 °C, the closer the prediction and the measured T_0 are to each other. In the low fluence region, the prediction seems to be 10–20 °C unconservative when applying $T_{0,SINTAP}$. In this region, the T_{0Q} values are closer to 0 °C. The uncertainty, σ, of the prediction is 22 °C which is larger than the observed differences. In high fluence region, the measured T_0 is significantly lower compared to the $T_{0,CVN}$ prediction.

Fig. 16 compares the results to the T_{41J} correlation, see Eq. (10). The same figure also shows that the relation between impact and fracture toughness for R4 and R3 welds follows the same trend as for B2 weld. The model developed in [18] for steels with varying content of Ni and Mn also follows the same trend. As the fluence increases, the shift in T_{41J} and T_{28J} tends to become larger in relation to ΔT_0, at least for high Ni/Mn steels.

$$T_{0CVN}(T_{41J}) = T_{41J} - 24 \pm 40 \tag{10}$$

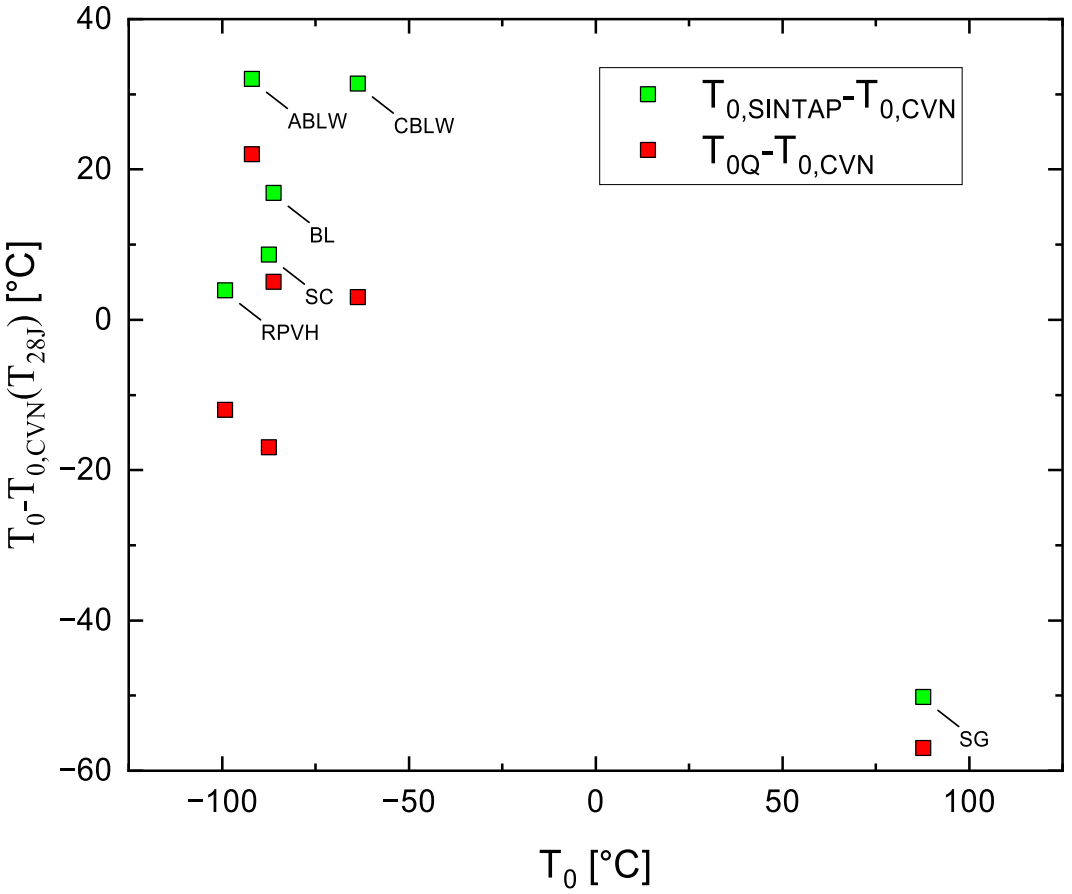

Fig. 15. Comparison of the T_0 prediction based on T_{28J} to the measured T_0. The figure includes both T_{0Q} and $T_{0,SINTAP}$ estimates.

4.5. Statistical upper bound embrittlement curves

Fig. 17 compares the upper bound embrittlement curves based on material and method uncertainties for T_{28J} and T_0. Fig. 17 shows that, despite the larger scatter bands of the T_0 curve, the T_0 method results still in a significantly lower curve compared to the CVN curve at high fluences. The upper bound of the impact toughness-based curve is based on the 2σ value resulting from the scatter in the T_{41J} parameters obtained from the surveillance program [11]. The T_0 upper bound curve presented in Fig. 17 is obtained by calculating T_{0eff} as described in [39] and adding the 1.44σ given in Table 4. The T_{0eff} term is the value providing the correct 5 % lower bound value due to inhomogeneity and σ gives the uncertainty of the method as described in ASTM E1921.

Due to the inhomogeneity, Fig. 10 shows that the MML method provides the most accurate description of the 5 % lower tail, equivalent to the upper bound of the presented embrittlement curve for T_0. The value providing the correct 5 % lower bound value is obtained when T_0 is 31 °C higher compared to the median T_0 embrittlement curve. The $\Delta T_{05\%eff}$ value is calculated using Eq. (11) [39].

$$\Delta T_{05\%eff} = \left(\frac{\sigma_{MML}}{6.6}\right)^2 + \left(\frac{\sigma_{MML}}{16.1}\right)^4 - \left(\frac{\sigma_{MML}}{19.4}\right)^6 + \left(\frac{\sigma_{MML}}{25.4}\right)^8 \quad (11)$$

In Eq. (11), σ_{MML} is set to 35 °C and comes from the combined assessment for the low fluence data, see Table 4 giving the σ_{MML} for a data set with 74 data points. In addition, the T_0 results are affected by the uncertainty of the method which is 1.44σ = 9 °C [39]. The margin adjusted $T_{05\%eff,MA}$ is 40 °C above the median embrittlement curve.

Because the embrittlement trend curve for B2 weld follows a general trend confirmed to be valid using other materials and σ_{MML} is determined for a large data set, the T_{0eff} can be determined in relation to the median curve. Otherwise, the uncertainty would be determined by using the point value at $F = 5.87 \bullet 10^{19} n/cm^2$ and using the method described in [39] for assessment of small data sets. As a result, the uncertainty would be larger as only 12 data points are applied to determine σ_{MML}.

5. Conclusions

Fracture toughness of high-Ni/Mn welds were characterized following ASTM E1921. The welds were extracted from a decommissioned power plant, Barsebäck 2, and its surveillance weld. The plant was operated for 23 effective full power years. The pressure

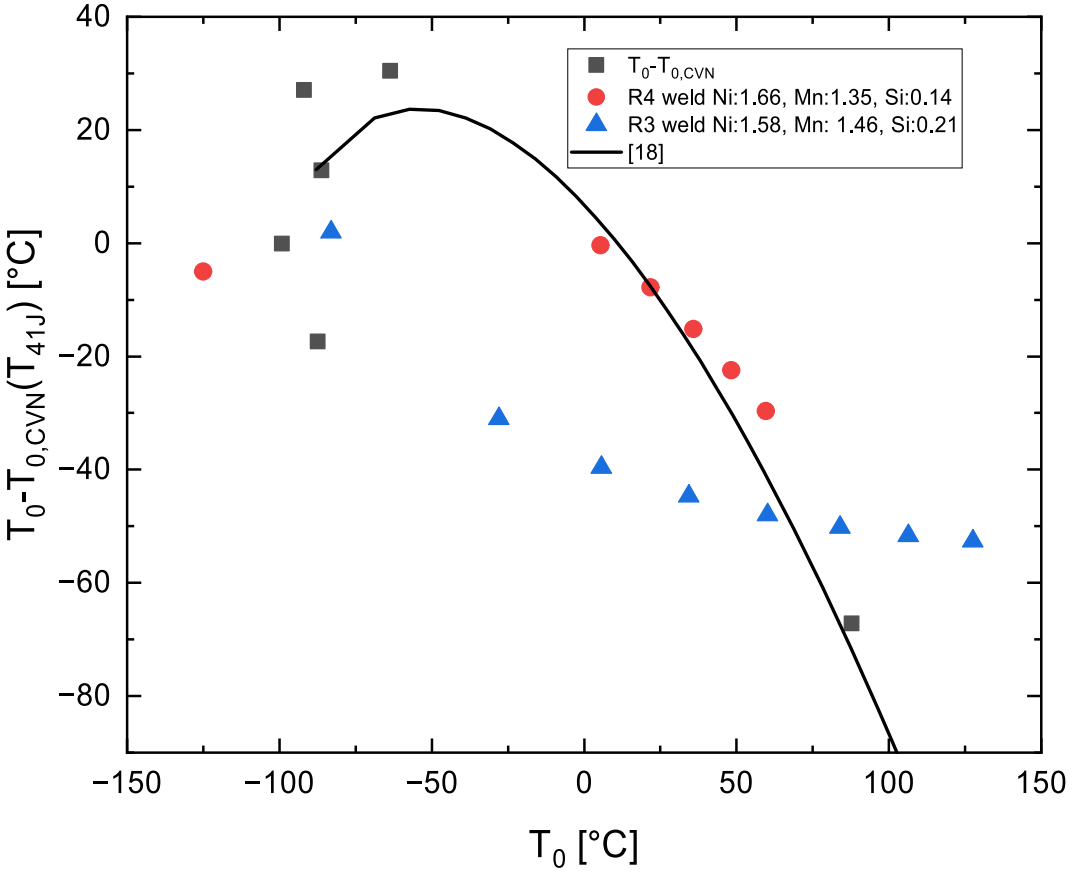

Fig. 16. Comparison of the T_0 prediction based on T_{41J} to the measured T_0. The behavior of B2 weld is compared to similar welds from R3 and R4 surveillance programs.

vessel materials were characterized at ¼ T location. Most of the welds are subjected to a low fluence ($< 0.102 \bullet 10^{19}$n/cm^2), but one of the investigated surveillance welds is subjected to a fluence of $5.87 \bullet 10^{19}$n/cm^2. The low fluence region contains the axial and beltline welds, surveillance weld C, and the non-irradiated RPVH and baseline welds. The maximum fluence for the extracted RPV welds is $3.8 \bullet 10^{17}$n/cm^2. The results are compared to impact toughness results for the same material and embrittlement curves for similar welds.

- The T_0 results from the surveillance program describe the aging behavior of the RPV welds in the beltline and the head region after 28 years of operation.
- The embrittlement rate is in line with previous results for similar welds with similar chemical content.
- In the low fluence region, the uncertainty due to the inhomogeneity and the method are larger than the possible effects of irradiation embrittlement on fracture toughness. Only the surveillance weld with a fluence of $5.87 \bullet 10^{19}$n/cm^2 result in a significantly different T_0.
- For the welds in the low fluence region, the maximum difference in T_0 is 23 °C. The reason for the scatter appears to originate from the multilayer characteristics of the weld. For the RPVH weld, when the crack tip is in the as-welded region T_0 is −135 °C, and T_0 is 50 °C higher when the crack is in the reheated region. Consequently, T_0 depends on the ratio between the sampled as-welded and reheated regions ahead of the crack.
- The results indicate that the difference between fracture toughness based T_0 and impact toughness based T_{41J} increases with fluence. At $5.87 \bullet 10^{19}$n/cm^2, the measured difference between the values is 91 °C. The trend appears to be typical at least for high Ni/Mn materials.
- The upper bounds of the derived embrittlement curves based on fracture and impact toughness are compared. The upper bound of the fracture toughness-based curve is farther from the median curve due to the sensitivity to the inhomogeneity, but the curve is still below the impact toughness-based curve.

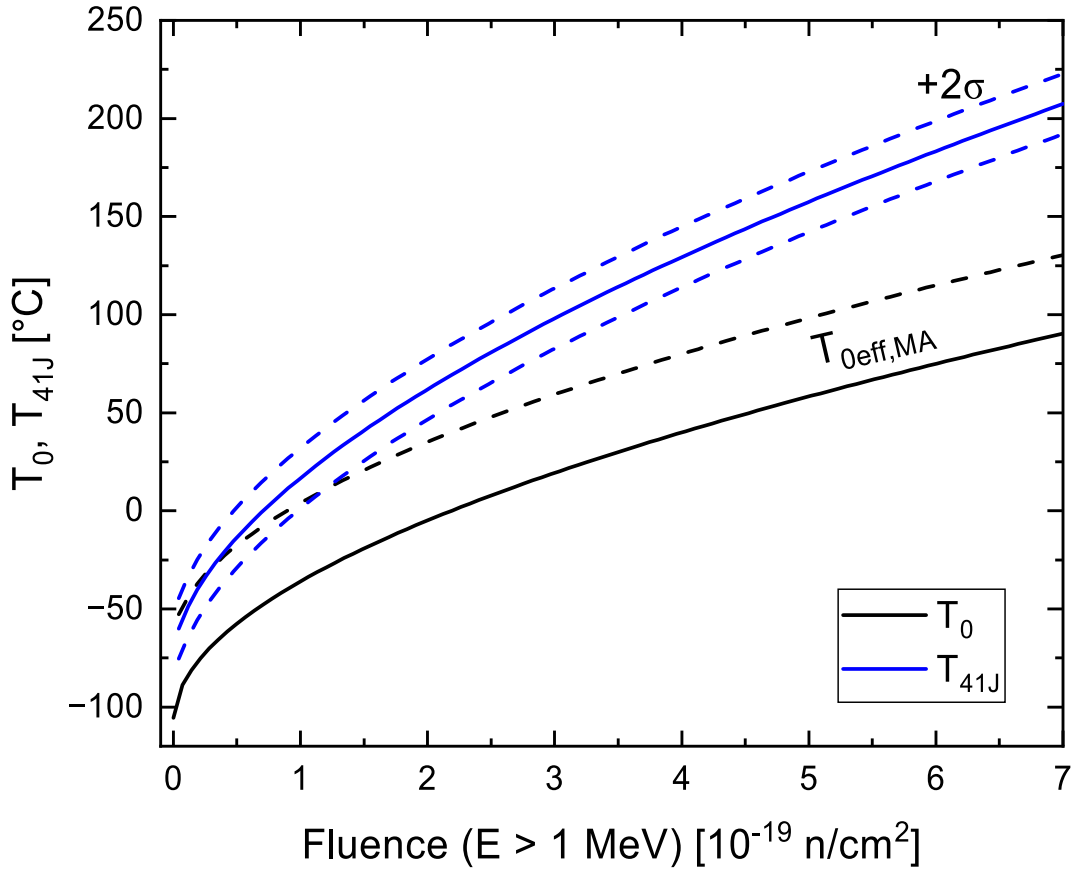

Fig. 17. Comparison of upper bound and median curves based on fracture toughness and impact toughness. The scatter in T_0 estimate is higher but the upper bound stays below the impact toughness based curve.

CRediT authorship contribution statement

Sebastian Lindqvist: Writing – original draft, Formal analysis, Conceptualization. **Noora Hytönen:** Writing – review & editing, Project administration.

Declaration of competing interest

The authors declare that they have no known competing financial interests or personal relationships that could have appeared to influence the work reported in this paper.

Acknowledgements

The funding for the research work is from the Finnish National Nuclear Safety and Waste Management Research Programmes SAFIR2022 and SAFER2028 realized through the dedicated projects BRUTE (2022) and BRIGHT (2025). The authors want to thank and acknowledge BREDA (Barsebäck RPV Research&Development Arena) of the substantial in-kind contribution for providing the research material. The authors want to thank Ringhals for providing the field service of extracting the material. Thank you to Pål Efsing and Johan Blomström for providing feedback. The Nordic nuclear safety research forum NKS is acknowledged for additional funding to support the Nordic collaboration in nuclear safety research.

Appendix 1:. Experimental work

Table A1 shows typical force–displacement curves for the characterized welds. Fig. A1 shows an example of the extracted C(T) specimens.

Table A1
Force-displacement curves.

RPVH, T = −126 °C, $K_{Jc,25mm}$ = 91 MPa$\sqrt{m}$

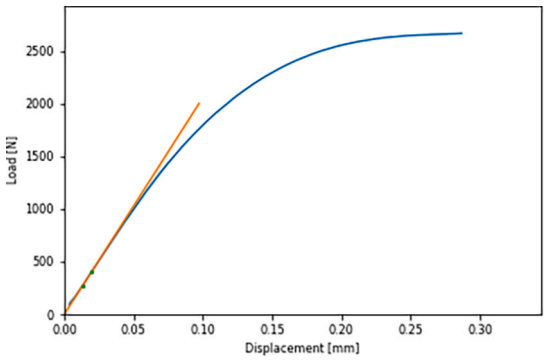

CBLW, T = −122 °C, $K_{Jc,25mm}$ = 85 MPa$\sqrt{m}$

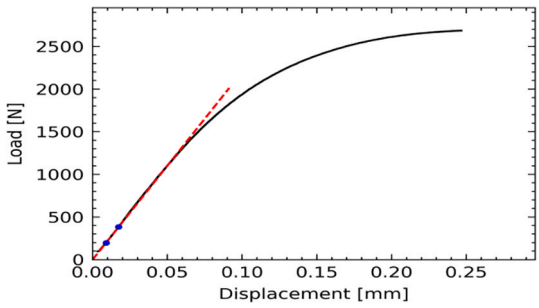

ABLW, T = −130 °C, $K_{Jc,25mm}$ = 93 MPa$\sqrt{m}$

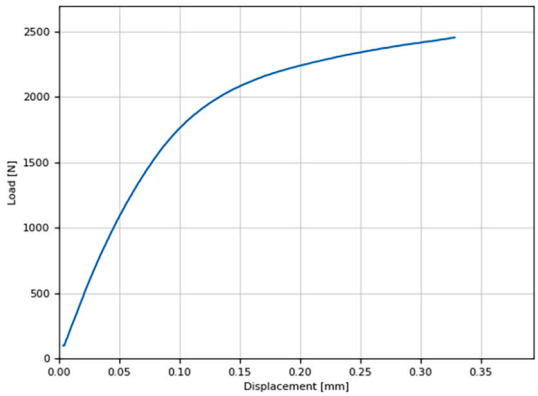

SC, T = −130 °C, $K_{Jc,25mm}$ = 92 MPa$\sqrt{m}$

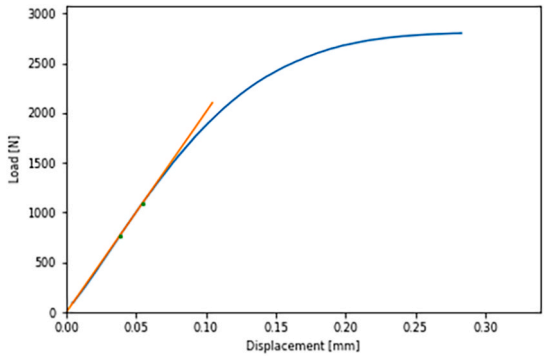

SG, T = −70 °C, $K_{Jc,25mm}$ = 96 MPa$\sqrt{m}$

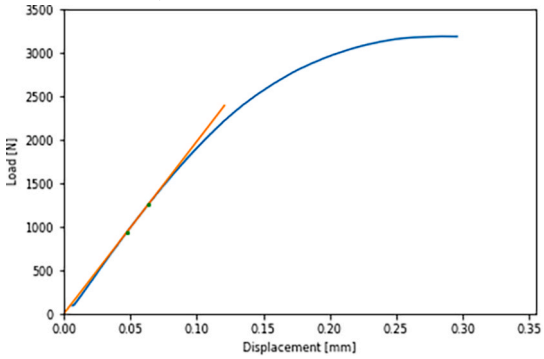

Fig. A1 shows the extracted C(T) specimens.

Fig. A1. Extracted C(T) specimens from a Charpy sized specimen.

Data availability

Data will be made available on request.

References

[1] W.L. Server M. Brumovský M. Kirk ASTM Symposium - Radiation embrittlement trend curves and equations and their use for RPV integrity evaluations 2023 Prague, Czech Republic., ASTM 10.1520/STP1647-EB.
[2] IAEA, Integrity of reactor pressure vessels in nuclear power plants: Assessment of irradiation embrittlement effects in reactor pressure vessel steels. N0. NP-T3.11, 2009. https://www-pub.iaea.org/MTCD/Publications/PDF/Pub1382_web.pdf.
[3] W.L. Server, Irradiation embrittlement of reactor pressure vessels (RPVs) in nuclear power plants, 2015. doi: 10.1533/9780857096470.1.3.
[4] Server WL, Brumovský M. International review of nuclear reactor pressure vessel surveillance programs. STP1603 2018. https://doi.org/10.1520/stp1603-eb.
[5] Astm. E185-16, Standard practice for design of surveillance programs for light-water moderated nuclear power reactor vessels. ASTM E185-16, ASTM. International 2016. https://doi.org/10.1520/E0185-16.Copyright.
[6] T.M. Rosseel, M.A. Sokolov, X. Chen, R.K. Nanstad, Current status of the characterization of RPV materials harvested from the decommissioned Zion unit 1 nuclear power plant, Proceedings of the Asme Pressure Vessels and Piping Conference, 2017, Vol 1B 3 (2017) 1–10. doi: 10.1115/PVP2017-65090.
[7] Sokolov MA, Nanstad RK. Fracture toughness characterization of midland beltline weld after high dose of irradiation. PVP2006-ICPVT11-93321 2008:1–5.
[8] D.E. McCabe, R.K. Nanstad, S.K. Iskander, D.W. Heatherly, R.L. Swain, Evaluation of WF-70 weld metal from the midland unit 1 reactor vessel. Oak Ridge National Laboratory. U S Nuclear Regulatory Commission. NUREG/CR-5736. ORNL/TM- 13748., 1998.
[9] Viehrig HW, Altstadt E, Houska M, Valo M. Fracture mechanics characterisation of the beltline welding seam of the decommissioned WWER-440 reactor pressure vessel of nuclear power plant Greifswald Unit 4. Int J Press Vessel Pip 2012;89:129–36. https://doi.org/10.1016/j.ijpvp.2011.10.016.
[10] Valo M, Ahlstrand R, Amaev DA, Krasikov EA, Kruykov A, Nikolaev V, et al. Characterization of the decommissioned Novovoronesh-1 pressure vessel wall materials by through-wall trepans. 19th ASTM Symposium of Effects of Radiation on Materials. 1998.
[11] Lindqvist S, Norrgård A, Arffman P, Hytönen N, Lydman J, Efsing P, et al. Mechanical behavior of Barsebäck 2 reactor pressure vessel welds after 28 years of operation. J Nucl Mater 2024.
[12] Hytönen N, Lydman J, Ge Y, Lindqvist S, Que Z, Efsing P. Microscopic characterisation of brittle fracture initiation in irradiated and thermally aged low-alloy steel welds of a decommissioned reactor pressure vessel. In Review, Journal of Nuclear Materials 603 2025. https://doi.org/10.1016/j.jnucmat.2024.155423.
[13] Blomström J, Roudén J, Efsing P. Experience with embrittlement trend curves in Swedish PWRs. ASTM Special Technical Publication STP 2023;1647:382–97. https://doi.org/10.1520/STP164720220067.
[14] May J, Rouden J, Efsing P, Valo M, Hein H. Extended mechanical testing of RPV surveillance materials using reconstitution technique for small sized specimen to assist long term operation. ASTM STP 2014;1576. https://doi.org/10.1520/STP157620130189.
[15] D. Erak, B. Gurovich, D. Zhurko, E. Kuleshova, A. Chernobaeva, V. Papina, O. Zabusov, A. Hodan, Improvement of radiation embrittlement dependences for VVER-1000 pressure vessel materials on service-life extension, SMiRT-23 (Structural Mechanics in Reactor Technology) Manchester, United Kingdom - August 10-14, 2015 (2015).
[16] Zarazovskii M, Revka V, Chyrko L. Chemical composition effect on radiation embrittlement and hardening of WWER-1000 RPV steels. ASTM Special Technical Publication STP 2023;1647:1–20. https://doi.org/10.1520/STP164720220079.
[17] Horizon, EU-project STRUMAT (Structural materials for nuclear safety and longevity) https://strumat-lto.eu/background/ 2020 Accessed: 1.7.2022, (2020).
[18] Lindqvist S, Kolluri M, David C, Zarazovskii M, Szabolcs S, Altstadt E. Fracture toughness behavior of steels with a fluence of 11·1019 n/cm2 and varying Ni/Mn content. In Review. Int J Press Vessel Pip 2024.
[19] Kryukov AM, Erak DY, Debarberis L, Sevini F, Acosta B. Extended analysis of VVER-1000 surveillance data. Int J Press Vessel Pip 2002;79:661–4. https://doi.org/10.1016/S0308-0161(02)00069-8.
[20] Vienna 2005.
[21] Davies L. A comparison of western and eastern nuclear reactor pressure vessel steels. Int J Press Vessel Pip 1999;76:163–208. https://doi.org/10.1016/S0308-0161(97)00075-6.
[22] Boåsen M, Lindgren K, Öberg M, Thuvander M, Faleskog J, Efsing P. Analysis of thermal embrittlement of a low alloy steel weldment using fracture toughness and microstructural investigations. Eng Fract Mech 2022;262. https://doi.org/10.1016/j.engfracmech.2022.108248.
[23] Kolluri M, Pierick P, Bakker T, Straathof BT, Magielsen AJ, Szaraz Z, et al. Influence of Ni-Mn contents on the embrittlement of PWR RPV model steels irradiated to high fluences relevant for LTO beyond 60 years. J Nucl Mater 2021;553:153036. https://doi.org/10.1016/j.jnucmat.2021.153036.
[24] Viehrig HW, Scibetta M, Wallin K. Application of advanced master curve approaches on WWER-440 reactor pressure vessel steels. Int J Press Vessel Pip 2006;83:584–92. https://doi.org/10.1016/j.ijpvp.2006.04.005.

[25] Wallin K, Nevasmaa P, Laukkanen A, Planman T. Master Curve analysis of inhomogeneous ferritic steels. Eng Fract Mech 2004;71:2329–46. https://doi.org/10.1016/j.engfracmech.2004.01.010.
[26] Chaouadi R, Schuurmans J. Critical analysis of the mini-CT geometry for fracture toughness characterization of the 73W high-copper submerged-arc weld in the unirradiated and irradiated condition. Eng Fract Mech 2024;298:109929. https://doi.org/10.1016/j.engfracmech.2024.109929.
[27] Que Z, Lindroos M, Lydman J, Hytönen N, Lindqvist S, Efsing P, et al. Brittle fracture initiation in decommissioned boiling water reactor pressure vessel head weld. J Nucl Mater 2022;569:153925. https://doi.org/10.1016/j.jnucmat.2022.153925.
[28] Hytönen N, Que Z, Arffman P, Lydman J, Nevasmaa P, Ehrnstén U, et al. Effect of weld microstructure on brittle fracture initiation in the thermally-aged boiling water reactor pressure vessel head weld metal. Int J Miner Metall Mater 2021;28:867–76. https://doi.org/10.1007/s12613-020-2226-6.
[29] Astm. E1921-23, Standard test method for determination of reference temperature, T0, for ferritic steels in the transition range. ASTM E1921-23 2023.
[30] Hernández Callejas R, Medina Almazán AL, Scibetta M, Vásquez Belmont S, Santillán Vergara M. Applying the Master Curve approach to a JRQ A533B Cl.1 material as part of the surveillance program of two BWR Units. Eng Fract Mech 119 2014:97–115. https://doi.org/10.1016/j.engfracmech.2014.02.014.
[31] Sánchez M, Cicero S, Arroyo B. Mini-C(T) specimens for Master Curve analysis of structural steels operating within their ductile-to-brittle transition region. Eng Fract Mech 2024;298:1–17. https://doi.org/10.1016/j.engfracmech.2024.109917.
[32] Bonny G, Altstadt E, Arffman P, Cicero S, Obermeier F, Petit T, et al. Present status of the FRACTESUS project: Round Robin on unirradiated materials. In: PVP2023-105449, ASME 2023 Pressure Vessels & Piping Conference; 2023. p. 1–9.
[33] M. Yamato, K. Onizawa, Y. Kentaro, T. Ogawa, Y. Mabuchi, M. Valo, M. Lambrecht, H.-W. Viehrig, N. Miura, N. Soneda, International round robin test on master curve reference temperature evaluation utilizing miniature C(T) specimens. Small specimen test techniques: 6th volume, 2015.
[34] M. Kocak, S. Webster, J.J. Janosch, R.A. Ainsworth, R. Koers, eds., FITNET - fitness for service - fracture, fatigue, creep, corrosion, 1st ed., Germany, 2008.
[35] Wallin K. Fracture toughness of engineering materials - Estimation and application. EMAS publishing 2011.
[36] Klein DV, Faleskog J. Influence of heterogeneity due to toughness variations on weakest-link modeling for brittle failure. Eng Fract Mech 2023;292:109643. https://doi.org/10.1016/j.engfracmech.2023.109643.
[37] D. Erak, B. Gurovich, E. Kuleshova, Y. Shtrombakh, D. Zhurko, V. Papina, Radiation embrittlement of VVER-1000 reactor pressure vessel materials., in: SMiRT-22, Conference on Structural Mechanics in Reactor Technology, 2013.
[38] Lindqvist S, Que Z, Nevasmaa P, Hytönen N. The effect of thermal aging on fracture properties of a narrow-gap Alloy 52 dissimilar metal weld. Eng Fract Mech 2023;281. https://doi.org/10.1016/j.engfracmech.2023.109056.
[39] K. Wallin, Assessment of Master Curve material inhomogeneity using small data sets. PVP2018-84297, American Society of Mechanical Engineers, Pressure Vessels and Piping Division (Publication) PVP PVP2018 (2018) 1–10. doi: 10.1115/PVP201884297.